Nuclear-magnetic-resonance relaxation rates for fluid confined to closed, channel, or planar pores

D. A. Faux and P. J. McDonald

Department of Physics, University of Surrey, Guildford, GU2 7XH, United Kingdom

Fast-field-cycling nuclear-magnetic-resonance (FFC NMR) experimentation measures the spin-lattice relaxation rate $T_1^{-1} = R_1$ as a function of NMR frequency f. It is a proven technique for probing the nanoscale dynamics of ^{1}H spins over multiple timescales. In many porous systems, fluid is confined to quasi-zero-dimensional (closed), quasi-one-dimensional (channel), or quasi-two-dimensional (planar) pores. Expressions are presented for $R_1(f)$ providing simulated dispersion curves for closed, channel, and planar pores where relaxation is associated with fluid movement relative to fixed relaxation centers in the solid. It is shown that fluid confined to nanosized (1–5 nm) spaces can be identified by submillisecond relaxation times for any geometry. The shape and magnitude of $R_1(f)$ is shown to be sensitive to pore geometry at low frequency only if relaxation is dominated by the motion of pore bulk fluid. Relaxation in most porous material is dominated by slow-moving surface fluid. Here, the pore geometry can only be distinguished if the relaxation center density is known *a priori* and then only at very low frequency. Systems containing mixtures of closed, channel, and planar pores of similar characteristic dimension h would present as three peaks at low frequency with closed pores providing the largest R_1 and planar pores the smallest. Pore size and shape variability in real systems is shown to diminish the ability to distinguish the three peaks. We show that the ratio T_1/T_2, where T_2 is the spin-spin relaxation time, is a complex function of h, the surface diffusion time constant τ_ℓ, and NMR frequency for $f > 1$ MHz. It is shown that measurements of T_1/T_2 at 20 MHz in cement paste and hydrocarbon rock capture information on both τ_ℓ and h.

I. INTRODUCTION

There are diverse porous material systems with important technological applications and properties dependent on the presence of proton-bearing fluid in nanometer-sized spaces. Examples include shales and mudstones which contain hydrocarbons and water mixtures, cement-based material for construction, biological and polymeric systems, zeolites for water desalination, purification, and catalysis, and wood and clays for waste storage. While standard experiments can assess the macroscopic behavior of confined fluid, for example through fluid-flow measurements, the options for probing the intrapore nanoconfined fluid directly and nondestructively are limited. Small-angle x-ray scattering [1–4] and quasielastic or small-angle neutron scattering [5–9] explore morphology and proton diffusion but rely on large facilities. Proton nuclear magnetic resonance (NMR) relaxation analysis is the most effective laboratory-based technique for probing the nanodynamics of spins in fluids, usually ^{1}H, contained in porous material. Nuclear magnetic resonance relaxometry measures the nuclear spin-lattice (longitudinal) or spin-spin (transverse) relaxation times of ^{1}H nuclei, T_1 or T_2, respectively. T_1 and T_2 depend on fluctuations in magnetic dipole-dipole interactions due to the relative motion of pairs of spins. Relaxation may arise due to the relative motion of like spins in the fluid, such as water or oil, the movement of fluid spins relative to relaxation centers at or close to the pore surfaces (for example, paramagnetic impurities), or motion relative to dissolved electronic spins such as aqueous paramagnetic impurity ions [6,10–28].

This article is concerned with fast-field-cycling NMR (FFC NMR) measurements which measure $T_1^{-1} = R_1$ as a function of Larmor frequency $\omega = 2\pi f$. Conventional NMR relaxation measurements, by contrast, use a fixed frequency normally in the range 1–40 MHz. The NMR frequency f is determined by the strength of the magnet and a fast-field-cycling NMR dispersion experiment adjusts the magnetic field and hence f accessing frequencies ranging from kHz to MHz. The broad frequency range accessible in a FFC NMR experiment means that, in principle, measurements capture information on the dynamical processes of fluid spins over timescales of picoseconds to microseconds. An excellent summary of methods and applications of FFC NMR is supplied by Steele and co-workers [29].

One difficulty with FFC NMR however is that $R_1(f)$ dispersion curves are difficult to interpret due to the complexity of fluid movement in the bulk and at the surfaces of pores of varied geometry and connectivity. The general strategy is to devise a simplified model that captures the key physics of the fluid dynamics in terms of a set of dynamical nanoscale time constants, to transform the model to a theoretical prediction of $R_1(f)$, and, finally, to fit to the experimental FFC NMR data. The process yields estimates of the chosen time constants which serve both to characterize the porous material and to provide insight into the dynamical processes at play.

Notable work by Korb, Kimmich, Levitz, and co-workers [10–15,18–20,26] in particular has pinpointed the dominant physical processes that lead to relaxation for a range of systems. In general, however, the models are sensitive to just a single nanoscale time constant when fitted to $R_1(f)$.

The time constant is normally τ_ℓ (alternatively labeled τ_m) which is the average time for a spin adsorbed to a pore surface to move a specified nanoscale reference distance δ (usually $\delta = 0.27$ nm—this being the "size" of a water molecule or the thickness of a water "layer"). We refer to τ_ℓ as the surface fluid diffusion time constant reflecting its simple relationship to the diffusion coefficient. Conventionally, the three-dimensional (3D) formula is employed for all diffusion time constants, namely $D = \delta^2/6\tau$. Separate measurement of the ratio T_1/T_2 at a spot frequency can be folded into a model to provide an estimate of the surface desorption time constant, τ_d (alternatively labeled τ_s). The nanoscale time constants τ_d and τ_ℓ provide a measure of fluid mobility at the surface and provide insight into surface diffusion mechanisms.

In previous papers, we were able to build on earlier work to develop a model that produces *three* time constants directly from a single dispersion curve without the need for separate measurements of T_1/T_2 [30,31]. These nanoscale time constants are τ_ℓ and τ_d as previously plus the pore bulk diffusion time constant τ_b. τ_b is conventionally defined as the time for water in the bulk of the pore to move a distance $\delta = 0.27$ nm and is related to the bulk diffusion coefficient by $D_b = \delta^2/6\tau_b$. τ_b provides the link to longer-range pore-to-pore transport. The model, called the 3τ model, was validated against plaster paste, synthetic clay, mortar, and oil-shale systems [30,31], providing fresh understanding of the dynamical processes which lead to spin relaxation. Simply, the 3τ model confirms that the complex dynamics of spins in pore spaces can be characterized by three time constants: one for the motion of spins across the surface, one for motion away from the surface, and one for the bulk fluid. Each of the three time constants is sensitive to different parts of the $R_1(f)$ dispersion curve.

The introduction of the 3τ model constituted an important step forward in the characterization of fluid-filled porous material because the three physical quantities τ_ℓ, τ_d, and τ_b characterize the *fluid* component of the system and are obtained from a *single* FFC NMR experiment. At the nanoscale τ_ℓ, τ_d, and τ_b may differ from pore to pore due to variations in pore surface chemistry, surface crystal orientation, surface steps, and the presence of impurities, to list but a few. Nonetheless, the time constants obtained from the 3τ model provide valuable *average* characteristic information for the *fluid* component of the porous system.

The 3τ model presented in Refs. [30] was developed for the restricted case of a fluid confined to a planar (quasi-two-dimensional or slab) pore of thickness h. Two important conclusions were reached. First, the ratio τ_ℓ/τ_d indicated that surface spins typically make less than 3 hops on the surface prior to desorption for all systems studied. Therefore surfaces need only be flat over distances 1 nm or so in order for the 3τ model to be valid. Second, the computed relaxation rates $R_1(f)$ for either the surface adsorbed fluid or the bulk fluid were found to be independent of h if $h > 5$ nm. The dipolar interaction between pairs of spins is short-range, decaying as a function of the spin-pair separation r as r^{-6}. Mobile spins farther than 5 nm from the surface containing relaxation centers collectively make a negligible contribution to the relaxation rate. This result effectively defines what is meant by "nanoscale thickness" in the context of a FFC NMR experiment.

However, while the 3τ model predicts that the separate relaxation rates $R_1(f)$ calculated for each of the surface adsorbed and bulk fluid components of a pore are independent of the planar pore thickness if $h > 5$ nm, the *measured* relaxation rates *are* sensitive to h through the surface-to-volume ratio. Over the timescale of a T_1 or T_2 measurement where $T_1, T_2 \gg \tau_\ell, \tau_d, \tau_b$ (the so-called biphasic regime, fast-diffusion region, or fast-exchange limit [32]) the spins in each fluid ensemble mix so that spins sample both environments. The measured relaxation rates are therefore the sum of the two separate relaxation rates weighted by the fraction x_i of spins in the ith environment. The relaxation rates associated with each of the surface and bulk environments are sensitive to that environment and so the measured relaxation rates are sensitive to x and hence to the characteristic dimension h for the pore. If, on the other hand, the two spin ensembles do not mix over the timescale of T_1 or T_2 (the slow exchange regime), the measurement will identify two separate relaxation rates. Thus FFC NMR can potentially identify both the characteristic dimension h for the porous material and identify fluid components in nonmixing environments.

In porous systems, fluid may occupy a range of physical environments each with distinctive diffusive properties offering differing $R_1(f)$ responses. This is especially true of two important classes of porous material: oil-bearing rock and cementitious material. The complexity of tight-oil systems was demonstrated by Ma and co-workers [33] using nanoresolution x-ray tomography on a mudstone. These researchers noted structures over length scales from nanometers to microns. Water is known to be located in a variety of environments in cement-based material where the development of more durable, greener cement-based products has driven the need to understand the nanoscale water environment. Water may be trapped by quasicrystal layers in interlayer spaces of about 1 nm, in so-called gel pores typically 3–5 nm, and capillary spaces of up to microns in size.

In this article, we calculate the frequency-dependent R_1 and R_2 relaxation rates for closed, channel, and planar pores, for pores of characteristic dimension $h < 5$ nm. The sensitivity of dispersion curves to the pore geometry and to h is examined in detail. We explore whether, in principle and in practice, a FFC NMR experiment can distinguish pore geometry. Experimentally, it is found that T_1/T_2 is approximately 4 for cementitious systems (for example [23]) and in the range 5–10 for oil-bearing rock (see [26,28] and references therein). These results are not fully understood. Here we show that T_1/T_2 is a complex function of NMR frequency f, pore dimension h, *and* the surface diffusion time constant τ_ℓ.

Section II describes the calculation of R_1 and R_2 for cuboidal closed pores, channel pores of rectangular cross section, and planar pores. The results are presented in Sec. III in which the dipolar correlation function R_1 and the ratio T_1/T_2 are presented. The conclusions are presented in Sec. IV.

II. THEORY

The spin-lattice and spin-spin relaxation rates, $R_1 = T_1^{-1}$ and $R_2 = T_2^{-1}$, respectively, are calculated for mobile fluid proton spins confined to Q0D (closed) and Q1D (channel) spaces. The expressions yielding R_1 and R_2 for a Q2D (slab

or planar pore) space were presented in Refs. [30,31] and are reproduced for completeness in Sec. II D. Here we use the notational convention that the dimensionality n in QnD refers to the number of non-nanoscale dimensions. Thus a Q0D space is nanosized in all three directions.

The analysis adopts the procedure established in standard texts [34–36] and developed in later works [30,31,37,38]. In this work, the relaxation is assumed to be dominated by the dipolar interaction of the confined mobile ^{1}H protons with fixed rare electronic paramagnetic impurity spins present in the pore matrix. The equations are equally applicable to systems where paramagnetic impurities are absent and relaxation is due to surface relaxation centers such as bonded hydrogen or F centers.

The relaxation rates are [23,34]

$$T_1^{-1} = R_1 = \tfrac{1}{3}\beta_{IS}[7J(\omega_S) + 3J(\omega_I)], \qquad (1)$$

$$T_2^{-1} = R_2 = \tfrac{1}{6}\beta_{IS}[4J(0) + 13J(\omega_S) + 3J(\omega_I)], \quad (2)$$

where $\beta_{IS} = (\mu_0/4\pi)^2\gamma_I^2\gamma_S^2\,\hbar^2 S(S+1)$; γ_S (γ_I) is the gyromagnetic ratio for the paramagnetic impurity (I spin) with $S = \tfrac{5}{2}$ for the common paramagnetic impurities Fe^{3+} and Mn^{2+}. The Larmor angular frequency of the impurity spin in the applied static field is $\omega_S = 658.21\omega_I$ and $\omega = 2\pi f$. The powder-average spectral density functions $J(\omega)$ are obtained from the cosine Fourier transformation of the powder-average dipolar correlation function $G(t)$ which in turn is found from the expression [30,31,34,39]

$$G(t) = \frac{4\pi}{5} \int_{\mathbb{R}^3} \int_{\mathbb{R}_0^3} \left[\sum_{M=-2}^{2} \frac{Y_{2M}(x_0, y_0, z_0)\, Y_{2M}^*(x, y, z)}{r_0^3\, r^3} \right]$$
$$\times P(\mathbf{r}, t \cap \mathbf{r}_0)\, d^3r_0 \; d^3r. \qquad (3)$$

Here $P(\mathbf{r}, t \cap \mathbf{r}_0)$ is the probability density function describing the probability distribution of pairs of spins separated by $\mathbf{r}_0$ at $t = 0$ *and* by $\mathbf{r}$ at time t. The subscript 0 on all quantities indicates the value at $t = 0$.

Equation (3) incorporates powder averaging assuming a uniform distribution of randomly oriented pores reflecting the usual experimental practice of using powdered samples [39] or accepting that unpowdered samples comprise large numbers of pores assumed to be randomly oriented within. The Y are the spherical harmonic functions of degree 2 (where the asterisk superscript represents the complex conjugate) expressed in terms of the Cartesian coordinates of the spin-pair vectors, $d^3\mathbf{r} \equiv dx\,dy\,dz$ and $r^3 = (x^2 + y^2 + z^2)^{3/2}$. Cartesian coordinates are used because the Q0D pore is cuboidal and the Q1D pore is a channel with a rectangular cross section. Alternative geometries (cylindrical for instance) lead to a significant increase in mathematical complexity associated with describing the spin-pair vector constraints, reiterating that the vectors $\mathbf{r}$ represent spin-pair vectors and not the coordinates of points in the pore space.

The distribution of relaxation centers, usually paramagnetic impurity spins located in the crystal, is represented as a single effective layer located close to the pore-crystal interface at a distance d from the front face of the pore fluid. The use of an effective layer of paramagnetic impurity spins aligns with
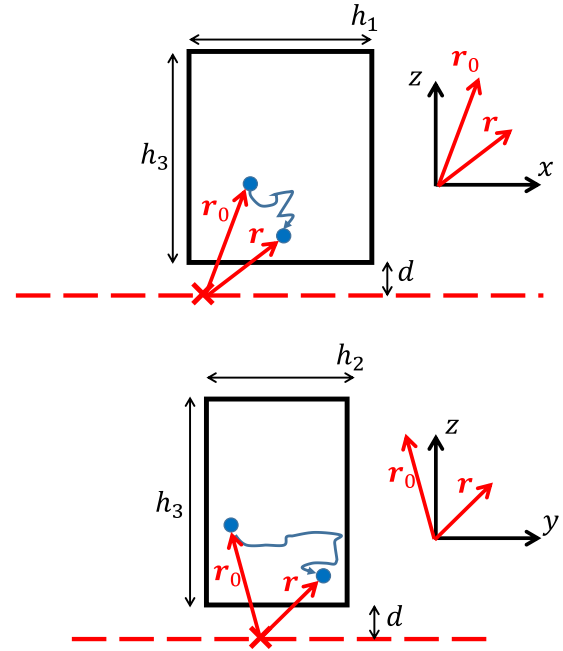
FIG. 1. A schematic diagram is presented of a cuboidal closed pore in which the fluid is contained in a region $h_1 \times h_2 \times h_3$. The upper and lower panels show the projections of the spin-pair vectors in the (x, z) and (y, z) planes, respectively, at $t = 0$ ($\mathbf{r_0}$) and at time t ($\mathbf{r}$). The dashed lines (red) represent the effective layer of paramagnetic spin density of size $3h_1 \times 3h_2$ placed a distance d from the fluid volume. The cross (red) indicates a paramagnetic impurity and acts as the origin of the spin-pair coordinate system (x, y, z) for the particular spin pair illustrated.

previous practice (for example, [13,26,31]). The underlying assumption is of a uniform distribution of relaxation centers characterized by N_f, the number of relaxation centers per unit volume. N_f acts as a linear scaling parameter in executing fits of a model to experimental data. But, at high relaxation center densities, the measured relaxation rates may not scale linearly with N_f due to clustering of relaxation centers in the solid. Consequently, the value of N_f emerging from a fit to an experimental dispersion curve may or may not align with a measured value of N_f.

The extent of the effective layer is the minimum size that ensures a uniform *a priori* probability of a time-zero spin-pair vector. With reference to the top diagram in Fig. 1 where the cuboidal pore has dimension h_1 in the x direction, this criterion is achieved if the extent of the centrally placed effective layer of paramagnetic impurity spins indicated by the dashed red line is $3h_1$ in the x direction (and $3h_2$ in the y direction). This requirement allows the conditional probability density function $P(\mathbf{r}, t \cap \mathbf{r}_0)$ to be written

$$P(\mathbf{r}, t \cap \mathbf{r}_0) = P(\mathbf{r}_0)P(\mathbf{r}, t \mid \mathbf{r}_0)$$
$$= N_f\, P(x, t \mid x_0)\, P(y, t \mid y_0)\, P(z, t \mid z_0) \quad (4)$$

for each system where $P(x, t \mid x_0)$, for example, is the time-dependent probability density function describing a pair of spins separated by distance x at time t *given* that the pair were separated by x_0 at $t = 0$. The particular choice of effective paramagnetic layer described in the sections below ensures

that the *a priori* probability density describing the probability per unit volume of finding a pair of spins, $P(\mathbf{r}_0) = N_f$, is constant, where N_f is the number of fixed paramagnetic impurity spins per unit volume within the solid. The effective paramagnetic layer in Fig. 1, for example, is therefore exactly as presented as a plane of size $3h_1 \times 3h_2$.

The spherical harmonic functions in Eq. (3) are expressed in Cartesian coordinates and simplified to yield

$$G(t) = \frac{N_f}{2} \int_{\mathbb{R}^3} \int_{\mathbb{R}^3_0} \frac{F(x_{0i}, x_i)}{r_0^5 \, r^5} \prod_{i=1}^3 P(x_i, t \mid x_{0i}) \, dx_{0i} \, dx_i,$$

(5)

where

$$F(x_{0i}, x_i) = 6 \sum_{\substack{i, j = 1 \\ j > i}}^3 x_{0i} x_i x_{0j} x_j$$

$$+ 2 \sum_{i=1}^3 x_{0i}^2 x_i^2 \; - \sum_{\substack{i, j = 1 \\ i \neq j}}^3 x_{0i}^2 x_j^2,$$

(6)

and where the alternative notation $x_1 \equiv x$, $x_2 \equiv y$, $x_3 \equiv z$ is used temporarily for succinctness.

The task is therefore to identify, for each pore system, the three probability density functions $P(x_i, t \mid x_{0i})$, substitute these expressions into Eq. (5), compute $G(t)$, and execute the Fourier transform, before, finally, determining the relaxation rates through Eqs. (1) and (2). For each of the closed, channel, and planar pores considered in Secs. II A–II D below, the probability density functions are fully defined by five parameters: the volume $h_1 \times h_2 \times h_3$ of pore space occupied by the mobile spins, the distance d of the volume from the effective layer of fixed paramagnetic relaxation centers contained in the solid, and the diffusion coefficient of the spins characterized by a time constant τ.

A. The closed (Q0D) pore

The geometry of the closed pore is illustrated in Fig. 1. The pore is cuboidal with dimensions $h_1 \times h_2 \times h_3$. The effective layer of paramagnetic impurities is centrally placed at a distance d below the pore face with dimensions $3h_1 \times 3h_2$ as previously justified. The probability density function $P(z, t \mid z_0)$ is found by a standard solution to the diffusion equation with reflective boundaries [31,40] as

$$P(z, t \mid z_0) = \frac{1}{h_3} \left[1 + 2 \sum_{p=1}^\infty e^{-Dp^2\pi^2 t/h_3^2} \right.$$

$$\left. \times \cos \frac{p\pi(z - d)}{h_3} \cos \frac{p\pi(z_0 - d)}{h_3} \right], \quad (7)$$

where the Einstein diffusion coefficient $D = \delta^2/6\tau$ and other quantities are defined in Fig. 1. Note that, here as elsewhere, it is assumed that the rotation of molecular protons on a single molecule with respect to the magnetic field is captured within

the overall translational motion of the molecules characterized by the diffusion coefficient D.

The probability density function for $P(y, t \mid y_0)$ is

$$P(y, t \mid y_0) = \frac{1}{h_2} \left[\frac{1}{2} + \sum_{p=1}^\infty e^{-Dp^2\pi^2 t/h_2^2} \cos \frac{p\pi y}{h_2} \cos \frac{p\pi y_0}{h_2} \right],$$

(8)

with the expression for $P(x, t \mid x_0)$ obtained by replacing y with x and h_2 with h_1. These equations may be substituted into Eq. (5) and the dipolar correlation function $G_{\text{Q0D}}(t)$ computed. We can find no helpful alternative to a brute force numerical integration of the six-dimensional integrations of Eq. (5). Note that we use the notation $G_{\text{Q0D}}(t)$ to describe the dipolar correlation function for a volume of fluid in a closed pore associated with a *single* layer of paramagnetic impurities exactly as illustrated in Fig. 1.

It is useful to determine the short-time ($t \to 0$) limit of $G_{\text{Q0D}}(t)$ as a check of the numerical integration. The limit may be obtained by setting $P(x_i, t \mid x_{0i}) = \delta(x_i - x_{0i})$ in Eq. (5) yielding

$$G_{\text{Q0D}}(0) = N_f \int_{\mathbb{R}^3_0} r_0^{-6} \, d^3r_0,$$

(9)

a result that is self-evident once obtained. The low-frequency regime of a FFC NMR dispersion curve is dependent on the long-time behavior of $G(t)$. $G_{\text{Q0D}}(t \to \infty)$ is found by making the substitutions

$$P(x, t \to \infty \mid x_0) \to \frac{1}{2h_1}, \quad P(y, t \to \infty \mid y_0) \to \frac{1}{2h_2},$$

$$P(z, t \to \infty \mid z_0) \to \frac{1}{h_3},$$

(10)

so that

$$G_{\text{Q0D}}(t \to \infty) = \frac{N_f}{8h_1h_2h_3} \int_{\mathbb{R}^3} \int_{\mathbb{R}^3_0} \frac{F(x_{0i}, x_i)}{r_0^5 \, r^5} \, d^3\mathbf{r}_0 \, d^3\mathbf{r}.$$

(11)

Again, the values of $G_{\text{Q0D}}(0)$ and $G_{\text{Q0D}}(t \to \infty)$ are best obtained by executing the integrations numerically. The important physics emerges from Eq. (11) where it can be seen that $G_{\text{Q0D}}(t \to \infty)$ becomes constant, independent of time, at long times. This arises because the pore is closed, fluid cannot escape (in this model), and the spin-pair probability density functions become time independent. This is akin to the rigid-ion limit and leads to a frequency-independent R_1 at low frequencies. A good example is seen in the low-frequency portion of the R_1 FFC NMR curve in Ref. [13].

The dipolar correlation function $G_{\text{Q0D}}(t)$ is computed separately for bulk fluid spins and for the fluid spins at the pore surface. The relaxation rate may then be obtained in each case using Eq. (1). $G_{\text{Q0D}}(t)$ is a function of parameters (h_1, h_2, h_3, d, τ) for a cuboidal volume of fluid (surface or pore bulk) of dimensions $h_1 \times h_2 \times h_3$ at distance d from the paramagnetic layer moving with a diffusion time constant τ. Care is required in combining contributions to the relaxation rates within the fast-exchange approximation [32]. Figure 2 presents the model used here. The bulk fluid is contained in a
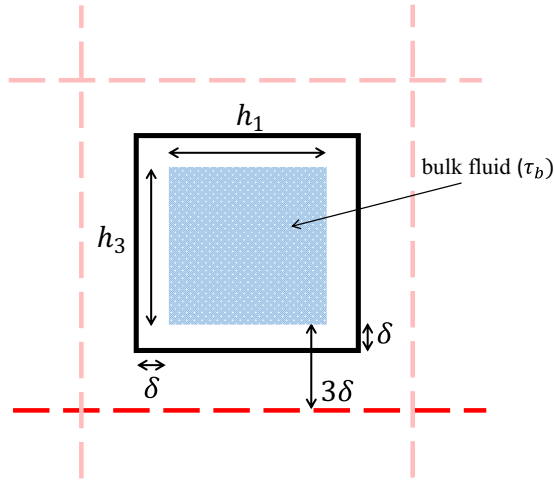
FIG. 2. A schematic diagram of a cuboidal closed pore of dimensions $h_1 \times h_2 \times h_3$ is presented showing the bulk fluid environment. The diagram shows the $x - z$ plane. The darker dashed line (red) represents the effective layer of paramagnetic spin density and has dimensions $3h_1 \times 3h_2$ as justified in the text. Equivalent paramagnetic layers are shown as lighter dashed lines (pink).

single volume with dimensions $h_1 \times h_2 \times h_3$. The calculation of $G_{\text{Q0D}}(t)$ via Eqs. (5), (7), and (8) is for a *single* layer of relaxation centers as illustrated in Figs. 1 and 2 but the *identical* ensemble of bulk spins interacts with each of the six layers of relaxation centers surrounding the cuboidal pore as illustrated in Fig. 2. Therefore

$$R_b = 2R_{\text{Q0D}}(h_1, h_2, h_3, 3\delta, \tau_b) + 2R_{\text{Q0D}}(h_3, h_1, h_2, 3\delta, \tau_b)$$
$$+ 2R_{\text{Q0D}}(h_2, h_3, h_1, 3\delta, \tau_b), \tag{12}$$

where R_b is the relaxation rate due to the fluid in the bulk of the pore.

The dipolar correlation function for the fluid at the pore surfaces is calculated by considering the relaxation associated with each of three surface ensembles A, B, and C with respect to a single effective layer of paramagnetic impurities as illustrated in Fig. 3. The surface fluid is assumed to comprise

FIG. 3. A schematic diagram of a cuboidal closed pore of dimensions $h_1 \times h_2 \times h_3$ is presented showing the surface fluid environments. The diagram shows the $x - z$ plane. The three assumed non-mixing surface layer ensembles are labelled A, B and C. The dashed line (red) represents the effective layer of paramagnetic spin density and has dimensions $3(h_1 + 2\delta) \times 3(h_2 + 2\delta)$.
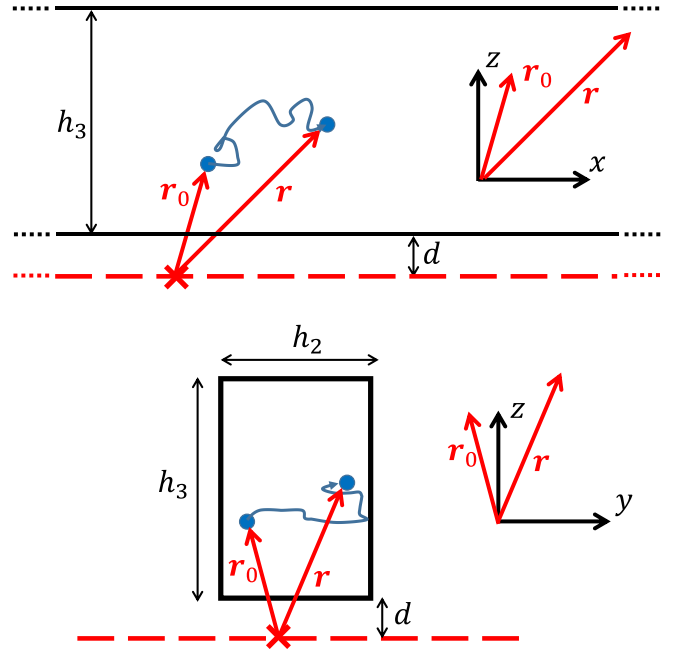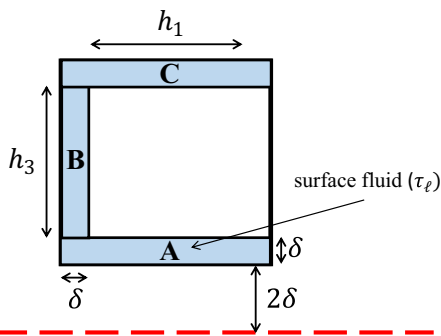
FIG. 4. A schematic diagram of a channel pore of infinite length in x and with a rectangular cross section of dimensions $h_2 \times h_3$ is presented. The upper and lower figures show the projections on the spin-pair vectors in the (x, z) and (y, z) planes, respectively, at $t = 0$ ($\mathbf{r_0}$) and at time t ($\mathbf{r}$). The cross (red) indicates a paramagnetic impurity and dashed lines (red) represent the effective layer of paramagnetic spin density placed a distance d from the pore.

a layer of thickness $\delta = 0.27$ nm, a distance large enough to accommodate a single water layer. The fluid adhered to the surfaces is assumed to comprise distinct, nonmixing ensembles. One ensemble, labeled A, is the layer closest to the effective layer of paramagnetic impurities and, with reference to Fig. 3, $R_A = R_{\text{Q0D}}(h_1, h_2, \delta, 2\delta, \tau_\ell)$. Ensemble B is a layer of fluid at the surface of the closed cuboidal pore at the side of the pore. For the specific ensemble B illustrated in Fig. 3, $R_B = R_{\text{Q0D}}(\delta, h_2, h_3, 3\delta, \tau_\ell)$. Four similar B ensembles exist for the closed cuboidal pore. Finally, ensemble C is the layer at the opposite face of the cuboidal pore to the layer of paramagnetic impurities considered in the calculation. Thus (see Fig. 3) $R_C = R_{\text{Q0D}}(h_1, h_2, \delta, 3\delta + h_3, \tau_\ell)$, and the relaxation rate for all six surface fluid components combined gives

$$R_\ell = R_{\text{Q0D}}(h_1, h_2, \delta, 2\delta, \tau_\ell) + 2R_{\text{Q0D}}(\delta, h_2, h_3, 3\delta, \tau_\ell)$$
$$+ 2R_{\text{Q0D}}(h_1, \delta, h_3, 3\delta, \tau_\ell)$$
$$+ R_{\text{Q0D}}(h_1, h_2, \delta, 3\delta + h_3, \tau_\ell). \tag{13}$$

B. The channel (Q1D) pore

A schematic diagram of the model channel pore is presented in Fig. 4. The channel pore has a rectangular cross section of dimensions $h_2 \times h_3$ and is infinite in extent in the x direction. The probability density functions $P(z, t \mid z_0)$ and $P(y, t \mid y_0)$ are given by Eqs. (7) and (8), respectively. The probability density function describing a pair of spins separated by distance x at time t given that the pair were

separated by x_0 at $t = 0$ is

$$P(x, t \mid x_0) = \frac{e^{-|x - x_0|^2 / 4Dt}}{(4\pi Dt)^{1/2}}. \tag{14}$$

Transformation of Eq. (14) into an integral equation via

$$P(x, t \mid x_0) = \frac{1}{2\pi} \int_{-\infty}^{\infty} e^{-Dtk^2} e^{-ikx_0} e^{ikx} \, dk \tag{15}$$

enables the integrations over x_0 and x to be undertaken analytically. This leads to

$$G_{\text{Q1D}}(t) = \frac{N_f}{2\pi} \int_0^{\infty} e^{-Dtk^2} \, dk \left[\iint_{\mathbb{R}^2} \iint_{\mathbb{R}_0^2} P(y, t \mid y_0) \, P(z, t \mid z_0) \right.$$
$$\left. \times X(y_0, y, z_0, z) \, d^2\mathbf{r}_0 \, d^2\mathbf{r} \right], \tag{16}$$

where

$$X(y_0, y, z_0, z) = \frac{8}{3} k^2 K_1'(kw_0) K_1'(kw) \left[1 + k^2 (y_0 y + z_0 z) \right.$$
$$\left. - \frac{2(y_0 z - z_0 y)^2}{w_0^2 w^2} \right]$$
$$+ \frac{8}{3} k^4 K_0(kw_0) K_0(kw) \left[1 - \frac{(y_0 z - z_0 y)^2}{2 w_0^2 w^2} \right]$$
$$+ \frac{8}{3} k^3 [K_0(kw_0) K_1'(kw) + K_0(kw) K_1'(kw_0)]$$
$$\times \left[\frac{1}{2} - \frac{(y_0 z - z_0 y)^2}{w_0^2 w^2} \right], \tag{17}$$

where $w^2 = y^2 + z^2$, $K_1'(kw) = K_1(kw)/w$, and K_0 and K_1 are modified Bessel functions of the second kind. Equation (16) has reduced two triple integrals to two double integrals at the cost of an integration over the Fourier variable k. The primary advantage of this approach, however, is that two troublesome numerical integrations over x_0 and x over the range $-\infty$ to $+\infty$ are avoided. All remaining integrations are evaluated numerically.

It is again useful to determine the dipolar correlation function $G_{\text{Q1D}}(t)$ in the limits of $t = 0$ and $t \to \infty$. As before, setting $P(x_i, t \mid x_{0i}) = \delta(x_i - x_{0i})$ yields

$$G_{\text{Q1D}}(0) = N_f \int_{\mathbb{R}_0^3} \frac{1}{r_0^6} \, d^3r_0, \tag{18}$$

but this time the integrations can be completed analytically. The final result is

$$G_{\text{Q1D}}(0) = \frac{\pi N_f}{12 \, h_2^3} [H(d) - H(d + h_3)], \tag{19}$$

where

$$H(z) = \frac{2z^4 + z^2 h_2^2 + 2h_2^4}{z^3 \sqrt{z^2 + h_2^2}}. \tag{20}$$

The long-time limit of $G_{\text{Q1D}}(t \to \infty)$ is proportional to $t^{-1/2}$ and found by taking the appropriate limits in real or Fourier space. Making the substitutions

$$P(x, t \to \infty \mid x_0) \to (4\pi Dt)^{-1/2},$$

$$P(y, t \to \infty \mid y_0) \to \frac{1}{2h_2}, \quad P(z, t \to \infty \mid z_0) \to \frac{1}{h_3} \tag{21}$$

into Eq. (5) followed by analytical integrations yields

$$G_{\text{Q1D}}(t \to \infty) = \frac{4N_f \sqrt{6\tau}}{3\sqrt{\pi} \, h_2 h_3 \delta} \left[\tan^{-1} \left(\frac{d}{h_2} \right) \right.$$
$$\left. - \tan^{-1} \left(\frac{d + h_3}{h_2} \right) \right]^2 t^{-1/2}. \tag{22}$$

The procedure for finding the separate relaxation rates associated with the bulk fluid (R_b) and the surface fluid (R_ℓ) follows that presented in Sec. II A with reference to Fig. 3. For the channel pore, which is infinite in extent in the x direction, $G_{\text{Q1D}}(t)$ for the bulk contribution is defined by the parameter set (h_2, h_3, d, τ) and so

$$R_b = 2R_{\text{Q1D}}(h_2, h_3, 3\delta, \tau_b) + 2R_{\text{Q1D}}(h_3, h_2, 3\delta, \tau_b). \tag{23}$$

For the surface fluid,

$$R_\ell = R_{\text{Q1D}}(h_2, \delta, 2\delta, \tau_\ell) + 2R_{\text{Q1D}}(\delta, h_3, 3\delta, \tau_\ell)$$
$$+ R_{\text{Q1D}}(h_2, \delta, 3\delta + h_3, \tau_\ell). \tag{24}$$

C. The line channel

It is useful to affirm the results emerging for the Q1D channel pore presented in Sec. II B with a simplified system. The line channel is unbounded in x (as for the Q1D channel) but has a square cross section sufficiently small so that the probability density function is uniform at all times in the y-z cross section. Thus it is sufficient to place $h_2 = h_3 = \delta$. In addition, the layer of paramagnetic impurities is infinite in extent in the y direction, rather than of dimension $3h_2$ for the full channel pore in Sec. II B. The benefits of exploring the line channel are that most integrations now become analytic, the key physics is clarified, and the solution serves as a check of the Q1D channel pore results in the limit of a narrow pore.

For the line channel,

$$P(z, t \mid z_0) = \frac{1}{\delta}, \quad \text{where} \quad z = z_0 = d, \tag{25}$$

$$P(y, t \mid y_0) = \delta(y - y_0), \tag{26}$$

$$P(x, t \mid x_0) = (4\pi Dt)^{-1/2} e^{|x - x_0|^2 / 4Dt}. \tag{27}$$

Equation (25) arises because there is only one value of z_0, d, regardless of the location of a paramagnetic impurity spin in the effective layer as can be seen in Fig. 4. The probability density is uniform across the nominal thickness δ of the line channel in the z direction. The expression for $P(y, t \mid y_0)$ in Eq. (26) arises because the y coordinate of spin-pair vectors will always be the same as y_0 regardless of how the spin moves along the line channel. However, the value of y_0 changes with the position of the paramagnetic impurity spin in the effective layer and so integration over y_0 is still required. $P(x, t \mid x_0)$ in Eq. (27) is the standard solution to the diffusion equation in 1D.

The equations (25)–(27) are substituted into Eq. (5) and simplified. The replacement of the real-space form of $P(x, t \mid x_0)$ of Eq. (27) using Eq. (15), executing the integrals

TABLE I. List of parameters.

Parameter	Value	Comments
β_{IS}	1.468×10^{-21} m^6/s^{-2}	Constant in Eqs. (1) and (2)
δ	0.27 nm	Nanoscale reference length
$d_{\sigma b}$	3δ	Distance from effective paramagnetic layer to bulk fluid
$d_{\sigma \ell}$	2δ	Distance from effective paramagnetic layer to surface fluid
N_f	1 spin/nm^3	Value chosen for presentation of $G(t)$ results
N_f	0.01 spins/nm^3	Value chosen for presentation of R_1 (typical for mortar/shale [13,26])
τ_b	20 ps	Diffusion time constant for bulk fluid [31]
τ_ℓ	0.1 μs	Diffusion time constant for surface fluid (except for Fig. 13)
τ_d	$= \tau_\ell$	Surface fluid desorption time constant

where possible, and simplifications yield

$$G_{\text{lc}}(t) = \frac{4N_f\delta}{3\pi} \int_0^\infty e^{-Dtk^2} k^2 dk$$
$$\times \int_{-\infty}^\infty \left[k^2 \, K_0^2(kw_0) + k \, K_0(kw_0)K_1'(kw_0) \right.$$
$$\left. + K_1'^2(kw_0) \, (1 + w_0^2k^2) \right] dy_0, \tag{28}$$

where $w_0^2 = y_0^2 + d^2$ and, as before, $K_1'(kw_0) = K_1(kw_0)/w_0$ and K_0 and K_1 are modified Bessel functions of the second kind.

The limits of $G(t)$ at $t = 0$ and $t \to \infty$ are found to be

$$G_{\text{lc}}(0) = \frac{\pi N_f \delta}{2d^4} \tag{29}$$

and

$$G_{\text{lc}}(t \to \infty) = \frac{N_f \sqrt{6\pi \tau}}{3d^3} t^{-1/2}. \tag{30}$$

D. The planar (Q2D) pore

The dipolar correlation function for mobile spins confined to an infinite plane of thickness h_3 was determined in Ref. [31]. The result is

$$G_{\text{Q2D}}(t) = \frac{4N_f}{5\delta^3\Delta} \int_0^\infty e^{-t\kappa^2/6\tau} \kappa \left[H(\kappa) + 2\sum_{p=1}^\infty E_p(t) \, C_p(\kappa) \right] d\kappa, \tag{31}$$

where $\kappa = k\delta$ is the dimensionless Fourier variable and $\Delta = h_3/\delta$ is the thickness of the Q2D fluid in units of δ. The functions are

$$E_p(t) = e^{-p^2\pi^2 t/6\Delta^2\tau}, \tag{32}$$

$$H(\kappa) = \frac{5\pi}{3}(e^{\kappa\Delta} - 1)^2 e^{-2\kappa(\Delta+\Gamma)}, \tag{33}$$

$$C_p(\kappa) = \frac{5\pi\kappa^4\Delta^4[e^{\kappa\Delta} - (-1)^p]^2 e^{-2\kappa(\Delta+\Gamma_{f\Upsilon})}}{3\,(\kappa^2\Delta^2 + p^2\pi^2)^2}, \tag{34}$$

where $\Gamma = d/\delta$ is the distance between the fixed spins and the fluid in units of δ. Note the minor correction in the numerator of Eq. (31) compared to Eq. (17) of Ref. [31].

The dipolar correlation function $G_{\text{Q2D}}(t)$ is determined by the parameter set (h_3, d, τ) and so, for the contribution due to the bulk fluid, we have

$$R_b = 2R_{\text{Q2D}}(h_3, 3\delta, \tau_b) \tag{35}$$

and, for the surface fluid,

$$R_\ell = R_{\text{Q2D}}(\delta, 2\delta, \tau_\ell) + R_{\text{Q2D}}(\delta, 3\delta + h_3, \tau_\ell). \tag{36}$$

III. RESULTS

The expressions presented in Sec. II permit the computation of $R_1(f) = T_1^{-1}(f)$ and $R_2(f) = T_2^{-1}(f)$ at NMR frequency f for Q0D (closed), Q1D (channel), and Q2D (planar) pores. Quantitative results are presented for relaxation due to the interaction of the mobile pore fluid with rare fixed paramagnetic impurities of spin $S = \frac{5}{2}$ contained in the solid. The calculations are easily adapted for surface relaxation centers, such as bound OH groups or F centers, by placing $d \approx \delta$ and changing β_{IS} as appropriate. Values of the parameters used in the present work are presented in Table I.

In the results that follow, the number of fixed paramagnetic spins per unit volume, N_f, is set to 1 for the purpose of generating results for the dipolar correlation function, $G(t)$, but $N_f = 0.01$ spins/nm^3 is assumed for the calculation of the relaxation rates so as to obtain quantitative estimates of the relaxation rates for systems in which relaxation is dominated by the presence of paramagnetic impurities. The latter is similar to both the effective density of Mn^{2+} paramagnetics in an oil shale sample [26] and also to the Fe^{3+} density in mortar [13]. The bulk diffusion correlation time $\tau_b = 20$ ps for all systems studied. In all applications of the 3τ model, τ_b was found to lie in the range 10–40 ps for water and 10–20 ps for light liquid alkanes [31]. Similarly, the range of values of τ_ℓ is chosen to be consistent with those emerging from fits to experimental data for a variety of porous systems [31].

Fluid contained in a pore with a dimension in excess of 5 nm yields relaxation times similar to that at 5 nm [30,31]. This is true whether or not a system is relaxed via the presence of paramagnetic impurities. Consequently, nanoscale dimensions, which are labeled by the symbol h, are set to values in the range 1–5 nm. The smallest dimension (1 nm) comprises about 4 "layers" of water. Thus a planar pore is characterized by a single nanoscale dimension $h < 5$ nm with the remaining two dimensions infinite in extent. The channel and closed pores have two and three nanoscale dimensions, respectively.
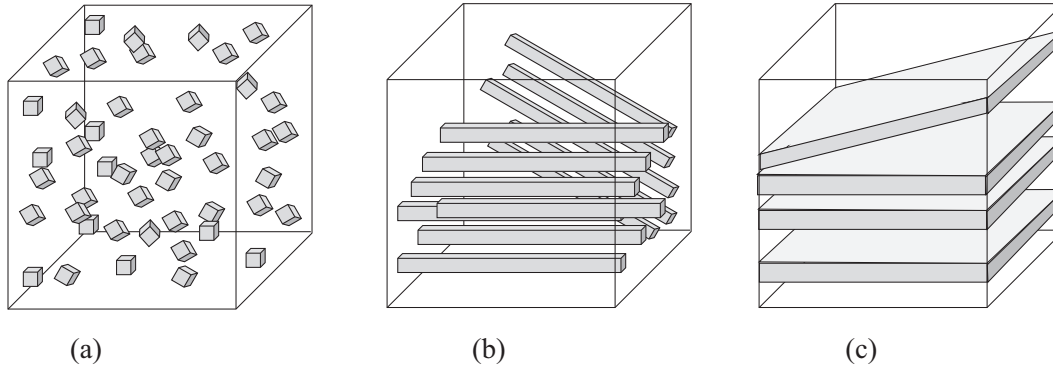
FIG. 5. Schematic diagram illustrating random orientation of identically sized (a) closed cubic pores, (b) channel pores with square cross section, and (c) planar pores.

A. $R_1(f)$ for bulk fluid in systems containing identical pore geometry

The first study explores the behavior of the dipolar correlation function $G(t)$ and spin-lattice relaxation rate $R_1(f)$ associated with the fast-moving bulk fluid confined to closed, channel, or planar pores. The contribution to $G(t)$ and $R_1(f)$ due to adsorbed slow-moving fluid at the pore surfaces is postponed until Sec. III B. The results presented in Figs. 6–11 are therefore directly applicable to systems in which the surface and bulk fluid have a similar diffusion coefficient ($\tau_\ell \approx \tau_b$), or when the surface layer is bound to the pore surface for timescales exceeding either T_1 or T_2 ($\tau_\ell > T_1, T_2$). The objective here is to establish the general characteristics of the dipolar correlation function $G(t)$ and the spin-lattice relaxation rate dispersion $R_{1b}(f)$ for each pore geometry and to check the computations against known limits.

The systems are illustrated in Fig. 5. Each system may contain pores which are differently oriented but are all identical in size. First, cubic closed pores are considered. The dipolar correlation function $G(t)$ was obtained by direct numerical integration of Eq. (5) using the probability density functions presented in Sec. II A. $G(t)$ is presented in Fig. 6(a) for cube side lengths of $h = 1$, 3, or 5 nm. $G(t)$ decays as t increases tending towards $G(t) \propto t^{-3/2}$ consistent with unconstrained 3D motion. The reflective boundary conditions come into play and in the long-time limit $G(t)$ is constant as expected for a closed pore. Vertical lines in Fig. 6(a) are placed at the point where the magnitude of the gradient of $G(t)$ is greatest. This provides an indicative time for the transition from 3D diffusion to 0D diffusion and is consistent with the time it takes, on average, for a spin to cross the pore, that is, to move a distance h.

The Fourier transform of $G(t)$ yields $J(\omega)$ and the relaxation rates are obtained via Eq. (1) as described in Sec. II A. The Fourier transform is calculated numerically for an integer number of cosine cycles such that the final cosine cycle terminates in the region where $G(t)$ is constant (to 3 significant figures over a time decade). The spin-lattice relaxation rate R_{1b} is presented as a function of frequency f in Fig. 6(b). The flattening of R_{1b} at low frequencies consistent with trapped fluid is clearly visible for cubic pores with dimensions $h < 2$ nm or less.

We now turn our attention to channel (Q1D) pore systems. The channels have square cross sections with side lengths of $h = 1$, 2, 3, 4, or 5 nm and are infinite in length. The dipolar correlation function $G(t)$ was evaluated by numerical computation of Eqs. (16) and (17) presented in Sec. II B. The dipolar correlation function $G(t)$ is presented in Fig. 7(a). At long times $G(t) \propto t^{-1/2}$ for channel pores, characteristic of 1D diffusion, but despite the rapid motion of the bulk fluid with a diffusion correlation time of $\tau_b = 20$ ps, the $t^{-1/2}$
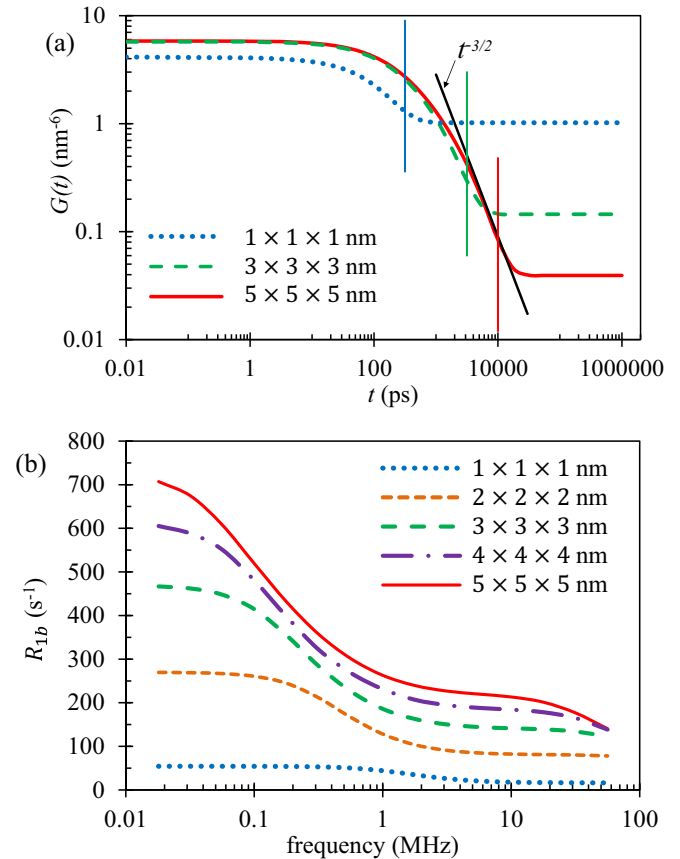
FIG. 6. (a) The dipolar correlation function $G(t)$ and (b) the spin-lattice relaxation rate R_{1b} are presented for a system of fluid-filled cubic closed pores. In (a), the vertical lines indicate the maximum magnitude of the gradient.
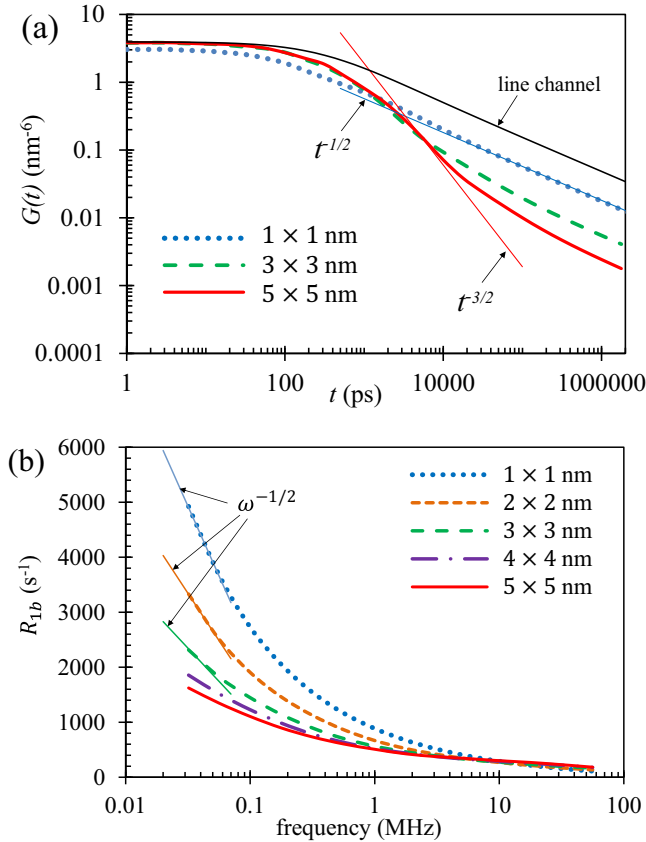
FIG. 7. (a) The dipolar correlation function $G(t)$ is presented for a system of fluid-filled channel pores with a square cross section. Guide slopes labeled $t^{-3/2}$ and $t^{-1/2}$ are provided as $G(t \to \infty)$ for 3D and 1D motion, respectively. Results for the line channel are also presented. The corresponding spin-lattice relaxation rate R_{1b} is presented in (b). The $\omega^{-1/2}$ form at low frequencies is shown for comparison. Parameters are indicated in Table I.

FIG. 8. (a) The dipolar correlation function $G(t)$ is presented for a system of fluid-filled planar pores of thickness h. Other parameters are indicated in Table I. A guide slope labeled t^{-2} is provided representing the long-time limit of $G(t)$. In (b), the corresponding spin-lattice relaxation rate R_{1b} is presented.

long-time limit is not reached until about 100 000 ps for the channel pores with 1×1 nm cross section. This result emphasizes the danger of taking a known long-time limit for $G(t)$ as a basis for a simplified diffusion model to yield $G(t)$. For comparison, the long-time limit $G(t) \propto t^{-3/2}$ for 3D bulk diffusion is shown as the red line in Fig. 7(a). The thickest pore, with cross section 5×5 nm, almost attains this limit before the effect of the pore walls is felt.

The equations for $G(t)$ for a simplified geometry, the line channel, were presented in Sec. II C and are also shown in Fig. 7(a) for comparison. Here, the cross section has dimensions $\delta \times \delta$ and the fluid is assumed to be uniformly distributed in the cross section at all times. The dipolar correlation function for the line channel has the same functional form as for the Q1D channels but is larger because the integrations in the y direction are executed analytically in Sec. II C over the range $-\infty < y, y_0 < \infty$ in contrast to the range $-h_2 < y, y_0 < h_2$ for the channel pore in Sec. II B.

The spin-lattice relaxation rate R_{1b} for the square cross-section channel pores is calculated from $G(t)$ as described in Sec. II B and presented in Fig. 7(b). The frequency dependence of R_{1b} is different from that of the closed pore

and the relaxation rates are higher. The dispersion curves are insensitive to channel pore size h at frequencies greater than 1 MHz. R_{1b} increases rapidly for the narrower pores at the lower frequencies because the probability of return of a spin to its position at $t = 0$ increases as the pore dimensions decrease. The low-frequency limit of the dispersion curve is determined by the long-time behavior of $G(t)$. For channel pores, $G(t) \propto t^{-1/2}$ as shown in Fig. 7(a) which leads to a $\omega^{-1/2}$ dependence of R_{1b} at low frequencies [41]. Sample $\omega^{-1/2}$ lines are drawn for $h = 1$, 2, and 3 nm pores in Fig. 7(b) and matched to the dispersion curve in each case. The dispersion curves are clearly tending to the $\omega^{-1/2}$ form at low frequencies but only at very low frequency. The larger channel pores will only reach this limiting form at frequencies $f \ll 20$ kHz. Figure 7 therefore highlights the danger of associating the functional form of the decay of a dispersion curve obtained from a FFC NMR experiment with a diffusion mechanism. The characteristic low-frequency behavior may only be seen outside the frequency range of the experiment.

The dipolar correlation function for planar pores is obtained from Eqs. (31)–(33) in Sec. II D and presented in Fig. 8(a). These calculations were originally produced in reference [31] and are presented here for ease of comparison.
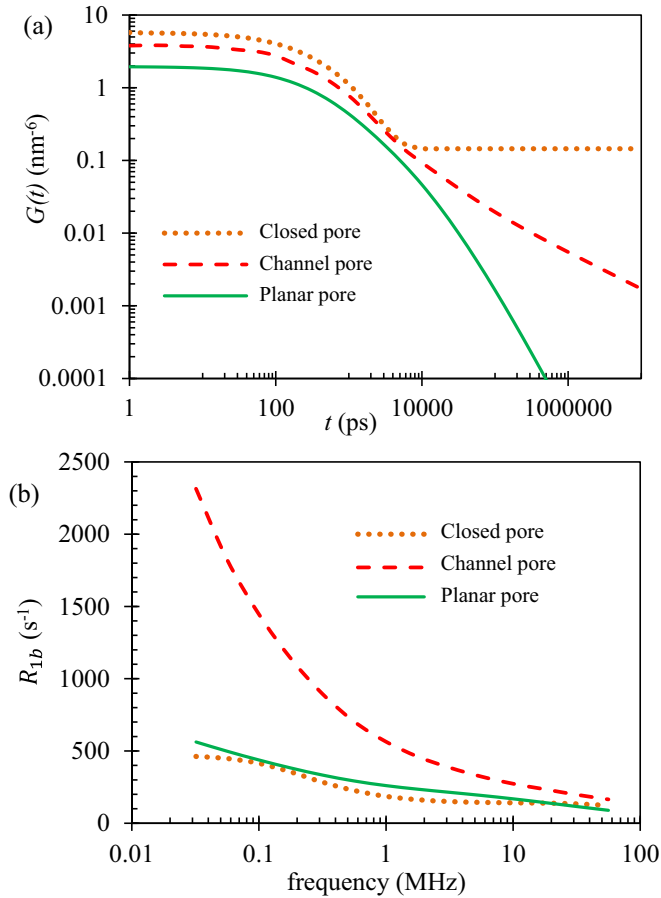
FIG. 9. (a) The dipolar correlation function $G(t)$ is presented for bulk fluid contained in a closed (orange dotted), channel (red dashed) and planar (green solid) pores of characteristic dimension $h = 3$ nm. In (b), the corresponding spin-lattice relaxation rate R_{1b} is presented.

For the planar pores, $G(t) \propto t^{-2}$ at long times as shown in Ref. [38] and proved in [31]. The reduced impact of the single boundary results in dipolar correlation functions which are only weakly dependent on h. Figure 8 presents the R_{1b} dispersion which correspondingly shows a weak pore-size dependence.

We now contrast and compare on the low-frequency limits of the R_{1b} dispersions for each pore geometry. Referring back to the closed pore, Fig. 6 clearly shows that R_{1b} is constant in the frequency range of a FFC NMR measurement for cubic closed pores of $h = 3$ nm or less. In the case of the channel pore, the expected constant low-frequency limit is only seen for the narrowest channels, that is, with a square cross section of $h \lesssim 2$ nm. For the planar pore, the expectation is that R_{1b} tends to a constant as $f \to 0$, as first demonstrated by Avogadro [42], but this is not apparent in Fig. 8. We have checked by calculating R_{1b} for very low frequencies and confirmed that the relaxation rate does indeed tend to a constant but that the flattening of the dispersion curve occurs only at frequencies less than about 10 kHz. Note that these rates are combined using Eq. (38) to find R_1. R_2 is found separately by the same method but using Eq. (2), and T_1/T_2 always tends to 1 at low frequency.

The effect of pore dimension is starkly revealed in Fig. 9. Figure 9(a) presents the dipolar correlation function for pores of different geometry but with a single characteristic dimension of 3 nm. Thus, a system of $3 \times 3 \times 3$ nm cubic pores is compared with a system of 3×3 nm channel pores and planar pores of thickness 3 nm. The initial $G(t)$ is similar for the closed, channel, and planar pores as spins decorrelate as for a 3D fluid. The impact of the 3 nm confining dimension(s) is not apparent at short times. The curves diverge at $t \approx 10\,000$ ps to adopt the long-time t^0, $t^{-1/2}$, and t^{-2} forms for closed, channel, and planar pores, respectively. The long-time behavior is clear in Fig. 9(b) which shows that the R_{1b} dispersion is similar at frequencies $f > 10$ MHz but has a strong dependence on geometry at low frequencies, especially for $f < 0.1$ MHz. This result suggests that measurements of R_1 at spot frequencies of order 10 MHz would not distinguish pore type even with the idealized systems represented in Fig. 9(a) but that FFC NMR can, in principle, make the distinction at frequencies less than 0.1 MHz where the dispersion shapes differ.

B. $R_1(f)$ for "real" systems

The dipolar correlation function $G(t)$ and the spin-lattice relaxation rate $R_1(f)$ for ideal closed, channel, and planar pores were presented Sec. III A assuming that relaxation was due to the interaction of the *bulk* fluid with a density of paramagnetic impurity spins contained in the pore walls. The numerical calculations were completed for a volume of fast-moving bulk fluid with a characteristic diffusion time constant $\tau_b = 20$ ps. The key physics responsible for the form of $G(t)$ and hence $R_1(f)$ for each pore type was explained and the numerical computations of the equations presented in Sec. II were checked against known limits. Having validated the equations presented in Sec. II and the subsequent computations, we now execute calculations using parameters typical of those obtained from the application of the 3τ model to FFC NMR dispersion curves from mortar and oil-bearing rock [13,26,30,31]. In these systems, it is known that the interaction of mobile ^{1}H spins with paramagnetic impurities dominates the relaxation rate.

The objectives are to establish whether it is possible in principle for a FFC NMR experiment to distinguish between pore geometry, to estimate the sensitivity of $R_1(f)$ to pore size and shape variation, and to demonstrate the dependence of the relaxation time ratio T_1/T_2 on NMR frequency f, surface diffusion time constant τ_ℓ, and characteristic pore size h. In doing so we acknowledge that real nanoporous systems contain fluid in pores with distributions of geometric shapes and sizes.

A system is presented schematically in Fig. 10(a). Relaxation is associated with the motion of spins in each of two environments. One contribution to the relaxation rate, labeled R_{1b}, is due to the interaction of the fixed relaxation centers in the solid and the fast-moving bulk fluid. The second, $R_{1\ell}$, is due to the interaction of the fixed relaxation centers with the fluid at the solid surfaces. The contribution due to surface fluid and bulk fluid spin interactions are negligible in comparison.

The contribution R_{1b} is calculated as described in Sec. II with results presented in Sec. III A. The relaxation
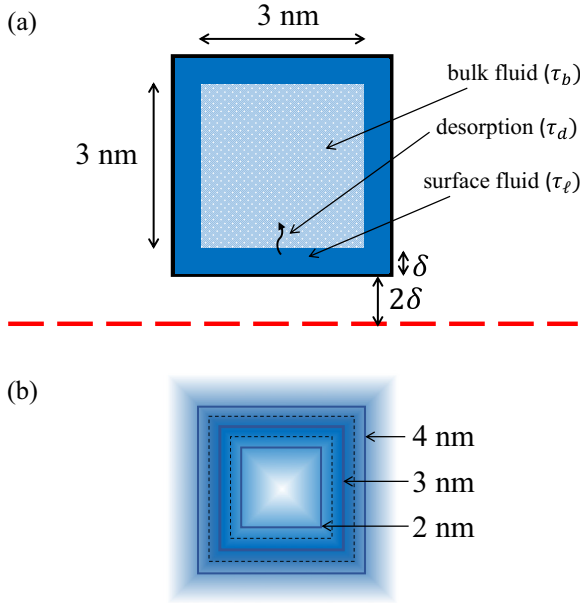
FIG. 10. (a) A schematic diagram of the system used to calculate R_1 comprising a combination of surface and bulk fluid. This schematic example is for a closed or channel pore of square cross section. Presented in (b) is a representation of a model pore with a mean dimension of 3 nm and a standard deviation of 1 nm.

associated with the interaction of the *surface* fluid of thickness $\delta = 0.27$ nm with the layer of paramagnetic impurities is calculated via $G_\ell(t, \tau_\ell)$ which is a function of the surface diffusion time constant τ_ℓ as described in Sec. II. The desorption time constant τ_d is introduced via an exponential decay term $\exp(-t/\tau_d)$ which describes the decay of the number of spins contained in the surface layer. A schematic diagram is provided in Fig. 10(a). Therefore

$$G_\ell(t, \tau_\ell, \tau_d) = G_\ell(t, \tau_\ell) \exp(-t/\tau_d) \tag{37}$$

by assumption which excludes the possibility of desorbed spins returning to the surface at a later time. This approach was fully justified in previous work with planar pores [30,31] because the pore thickness h was very large and the probability of return was negligible, but becomes less satisfactory for nanosized pores, especially for closed pores containing trapped fluid. The exponential in Eq. (37) decays to zero whereas of course it should decay to x, the fraction of spins at the surface. However, bearing in mind a number of other more significant uncertainties, particularly the choice of values for $\tau_\ell, \tau_d, \delta,$ and d embedded in the 3τ model, this approximation is of little consequence.

In the analysis that follows $\tau_b = 20$ ps (as previously) which is typical of water and hydrocarbons, and $\tau_\ell = \tau_d = 100$ ns typical of values seen in previous work [31]. Note that $\tau_\ell = \tau_d \gg \tau_b$. The relaxation rate, in accordance with the fast-diffusion approximation [32], is then given by

$$R_1 = x R_{1\ell} + (1 - x) R_{1b}, \tag{38}$$

where x is the fraction of spins in the surface layer (equivalent to the surface-to-volume ratio) and where $R_{1\ell}$ and R_{1b} are the rates associated with the surface layer and bulk fluid respec-
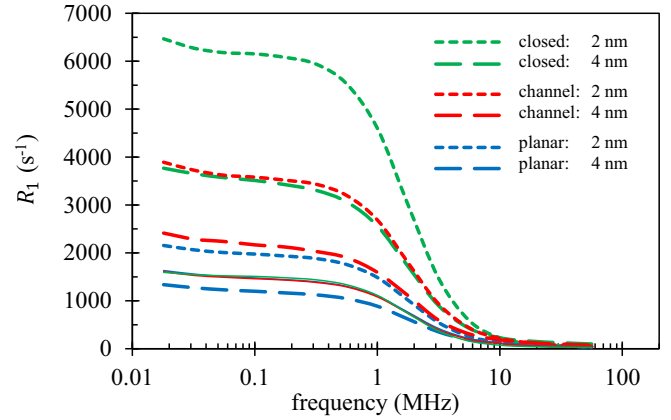
FIG. 11. The spin-lattice relaxation rate R_1 dispersion is presented for closed cubic pores (green curves with the largest R_1), channel pores with square cross-section (red curves) and planar pores (blue curves with the smallest R_1). In each case, the short dash (upper) and long dash (lower) curves are for nano-sized dimensions of 2 nm and 4 nm respectively. The solid lines (almost coincident) are for a nano-sized dimension of 3 nm but where the dispersion curves for the channel and closed pores assume different paramagnetic impurity densities as described in the text.

tively. An identical expression applies for R_2. All parameters are presented in Table I.

Figure 9(b) demonstrates that the shape of the R_{1b} dispersion is most sensitive to the pore shape at low frequencies (1 MHz or less). We now examine the sensitivity of $R_1(f)$ to pore geometry including the contribution from both bulk and surface fluid in accordance with Eq. (38). In addition, we determine the spread of R_1 for each pore type taking into account a reasonable pore-size variability by assuming that a sample contains pores with characteristic dimension h as a Gaussian distribution with a mean of 3 nm and a standard deviation of 1 nm as illustrated in Fig. 10(b). Thus, for closed pores $h_1 = h_2 = h_3 = 3$ nm with a standard deviation of 1 nm, similarly for the channel and planar pores. Taking the closed pore as an illustration, it is found that the relaxation rates for combinations of pore size for each of the three sides (h_1, h_2, h_3) are contained within the envelope formed by the minimum and maximum cube. Thus the relaxation rates formed of the cubes $(2,2,2)$ and $(4,4,4)$ contain $(2,2,4)$, $(2,3,4)$, $(3,4,4)$ and so forth for all combinations. Figure 11 therefore presents $R_1(f)$ for each of the closed, channel, and planar pores via two curves for $h = 2$ nm and 4 nm representing the range of relaxation rate for pores of characteristic dimension $h = 3$ nm with one standard deviation variation in pore dimension.

The results presented in Figs. 11 and 12 are computed for cubic closed pores, channel pores with square cross section, and planar pores. The variation of geometry for cuboidal pores, for instance, has been shown to be contained with the extremes of $2 \times 2 \times 2$ nm and $4 \times 4 \times 4$ nm pores. We argue that these results are also applicable to the wide range of pore geometries anticipated in real systems, such as cylinders, spheres, and ellipsoids, provided the maximum and minimum dimensions of the pore lie in the range 2–4 nm. Since $\tau_\ell \approx \tau_d$, the vast majority of spins at the surface of a pore will only execute 0, 1, or 2 hops within the surface (at most
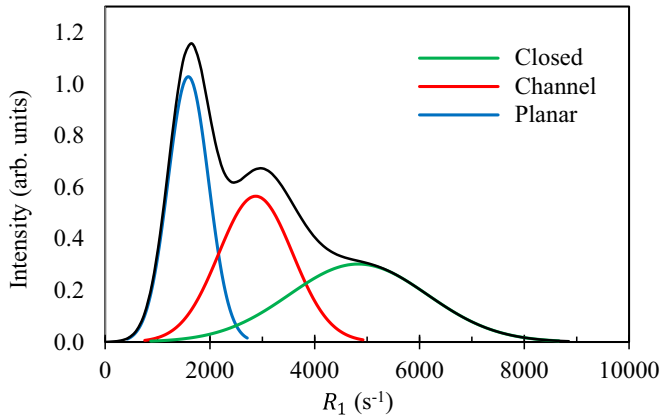
FIG. 12. The figure provides a simulated spin-lattice relaxation rate R_1 response from a system containing equal volumes of fluid in closed, channel and planar pores at a frequency $f =100$ kHz. The Gaussian curves are estimated for $h = 3 \pm 1$ nm pores for closed cubic pores (green and at right), channel pores of square cross-section (red and central) and planar pores (blue and at left) with the combined response (black).

0.5 nm) before desorption. Few spins will explore a jagged or curved surface prior to desorption and so the relaxation physics pertaining to alternative geometries will be captured by Figs. 11 and 12.

Figure 11 shows that the relaxation rates are high and the relaxation times are short, for all pore types. The dispersions are dominated by the contribution due to the surface spins. This is because these spins are closest to the paramagnetic spins located in the pore walls and because the diffusion and desorption of the surface mobile spins are slow compared to the movement of the bulk spins. Further, referring to Fig. 3, for closed and channel pores, $R_A \gg R_B \gg R_C$, and for planar pores $R_A \gg R_C$. Not only is $R_{1\ell} \gg R_{1b}$ but x, the surface-to-volume ratio, is larger for nanosized pores compared to thicker pores. Submillisecond relaxation times are indicative of nanoconfined fluid. Such short relaxation times are not easily accessible in FFC NMR measurements. However, the rates are proportional to the paramagnetic relaxation center density assumed here to be $N_f = 0.01$ spins/nm^3. R_1 is proportional to N_f and so a FFC NMR measurement might signal nanosized pores at low frequency if the density of paramagnetic relaxation centers is low.

The importance to the analysis of a supplementary measurement of the paramagnetic spin density is clearly evident for systems in which relaxation is dominated by this mechanism. The relaxation rates are also proportional to β_{IS} which in turn is proportional to the square of the gyromagnetic ratio and to the product $S(S + 1)$ where S is the spin of the relaxation center. The analysis presented here is easily adapted to systems without paramagnetic impurities, such as synthetic clays, plaster, biomaterials, and others where relaxation is dominated by surface relaxation centers including chemically bound protons at the pore surface, for example as OH groups.

The similarity of the *shape* of the dispersion curves in Fig. 11 is due to the dominance of $R_{1\ell}$ to the measured relaxation rate. The interaction of the slow-moving surface fluid with the layer of paramagnetic impurities is nearly indepen-

dent of pore geometry. To illustrate the point, three additional curves are presented: a 3 nm planar pore with paramagnetic spin density $N_f = 0.01$ spins/nm^3, a 3 nm channel pore with $N_f = 0.0054$ spins/nm^3, and a 3 nm closed pore with $N_f = 0.0034$ spins/nm^3. The three curves almost coincide.

In summary, the presence of nanosized pores is indicated by the high values of relaxation rate. Collectively, these results suggest that a system containing a mixture of fluid-filled cubic pores, channel pores of square cross section, and planar pores each with a characteristic nanodimension h will present in a FFC NMR experiment as three distinct peaks at low NMR frequencies with the highest, middle, and lowest R_1 associated with the closed, channel, and planar pores, respectively. If, on the other hand, a system contains pores of a single geometry, it would not be possible to identify the pore geometry (closed, channel, or planar) unless the paramagnetic spin density was known *a priori* (for instance by electron spin resonance measurement). As a note of caution, even if the paramagnetic spin density were measured, clustering in the solid or desorption of surface spins into the fluid may provide a different *effective* density of relaxation centers.

We now suppose that a sample contains a mixture of closed pores, channel pores, and planar pores each with a Gaussian distribution of the nanoscale dimension h with mean 3 nm and standard deviation of 1 nm. In principle, Fig. 11 shows that a FFC NMR measurement could identify the fluid in each pore type provided there was no movement of the fluid between pores types over the timescale of T_1 or T_2. Under these circumstances, three characteristic relaxation rates would be observed at low frequency with the highest rate associated with the closed pores, the second highest with the channel pores, and the smallest rate by the planar pores. The intensity of each peak would be proportional to the number of spins in each pore geometry.

Simulated measurement at a frequency of 100 kHz is presented in Fig. 12 for a mixed system with equal numbers of spins in planar, channel, and closed pores. Each peak is represented as a Gaussian distribution which approximates the spread of relaxation rate indicated in Fig. 11 for each geometry. The spread of R_1 is broad and it becomes difficult to distinguish the contributions from the separate pore type. Thus, variability of nanoscale pore size diminishes the ability of a FFC NMR experiment to identify pore type at low frequency.

C. The relaxation time ratio T_1/T_2

We now turn our attention to the ratio T_1/T_2 which is found from T_1-T_2 exchange measurements to be approximately 4 for white cement paste [23] and in the range 5–10 for oil-bearing rock (see [26,28] and references therein) at $f = 20$ MHz. The planar pore was used successfully within the 3τ model to fit to dispersion curves of mortar [13] and oil-bearing rock [26] and justified in Ref. [31]. We therefore calculate the frequency dependence of T_1/T_2 for a planar pore only for thicknesses $h = 3$, 30, and 100 nm and for surface diffusion time constants τ_ℓ of 100 ns, 200 ns, and 400 ns. Once again, $\tau_b = 20$ ps with $\tau_d = \tau_\ell$.

The ratio T_1/T_2 is presented in Fig. 13 and found to be a complex function of three variables: NMR frequency f, pore
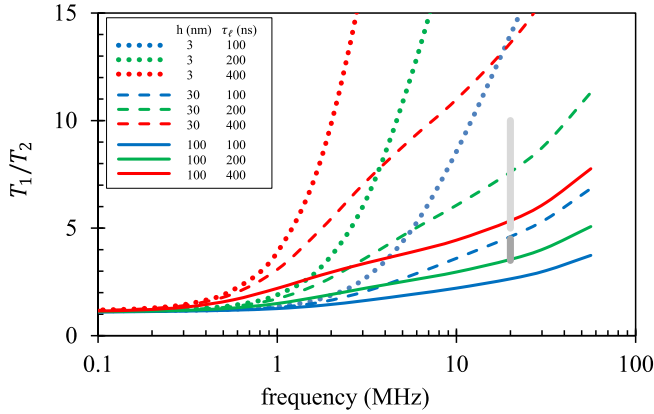
FIG. 13. The ratio T_1/T_2 is presented as a function of frequency for a selection of values of τ_ℓ and h for a planar pore. The vertical bars are at a spot frequency of 20 MHz and represent the range of T_1/T_2 ratio observed in cement pastes (lower bar) and hydrocarbon rock (upper bar).

thickness through x in Eq. (38) (the surface-to-volume ratio), and τ_ℓ. Figure 13 shows that T_1/T_2 is nearly 1 at frequencies below about 500 kHz but changes rapidly in the range $f > 1$ MHz typical of T_1-T_2 experiments. T_1/T_2 may be determined experimentally from T_1-T_2 exchange measurements undertaken at a spot frequency. The vertical bars at 20 MHz reflect the ranges of T_1/T_2 found in cement material and hydrocarbon rock. Each bar straddles a significant region of (τ_ℓ, h) space. T_1-T_2 exchange measurements at two or more spot frequencies would provide the critical information needed to characterize h and τ_ℓ for the material.

The ratio $T_1/T_2 \approx 4$ is approximately constant for various types of cement paste. Figure 13 shows that T_1/T_2 is least sensitive to h and to τ_ℓ at large values of h and long τ_ℓ. It has been suggested that the large values of T_1/T_2 observed from oil-bearing rock are due to the *bulk* diffusion of hydrocarbons within pores of reduced dimensionality [26,28]. The results presented here show that this is not the case. We have shown that regardless of pore geometry, the relaxation rate response is dominated by the monolayer of *surface* fluid. This is true regardless of pore geometry as demonstrated in Fig. 11.

T_1/T_2 is also cited as being linked to "surface affinity." Surface affinity is defined in terms of energy and is a property of the energy of interaction of a droplet of fluid with both the solid surface and the fluid that surrounds it. We find that T_1/T_2 is strongly dependent on τ_ℓ. τ_ℓ is a measure of surface *mobility* which is most certainly related to surface affinity. Consequently, we agree that T_1/T_2 is linked to surface affinity through τ_ℓ but not in a simple way due to the additional complex dependence on h and f. It is *not* the case that T_1/T_2 can be used as a measure of surface affinity but a direct measure of surface *mobility* can be obtained from FFC NMR measurement analyzed using the 3τ model to find τ_ℓ.

IV. CONCLUSIONS

The equations allowing computation of the dipolar correlation function $G(t)$ and hence the spin lattice (longitudinal) and spin-spin (transverse) NMR relaxation rates, R_1 and R_2, are presented for closed and channel pores. The frequency dependence of R_1 and R_2 is computed for ^{1}H-bearing fluid contained in nanosized closed, channel, and planar pores for relaxation associated with spin motion relative to fixed relaxation centers contained in the solid. The computations are validated against known limiting forms for the bulk fluid component of filled pores. The results for $R_1(f)$ for cubic closed pores of dimension $h = 1$–5 nm containing only bulk fluid exhibit high pore-size dependence and flattening of the dispersion curve at low frequencies consistent with the presence of spins confined to a volume of space for a time period longer than T_1 or T_2. The $R_1(f)$ dispersions curves for channel pores of square cross section containing bulk fluid with h in the range 1–5 nm show sensitivity to h at frequencies less than 100 kHz. Planar pores have a weak sensitivity to pore size.

The relaxation rates for a surface layer of fluid using the same expressions derived in Sec. II are calculated and combined with the contribution due to the bulk fluid to provide simulated $R_1(f)$ dispersion for realistic closed, channel, and planar pores. The presence of fluid in nanosized pores is characterized by very high rates at low frequencies. Relaxation times would be submillisecond at frequencies less than about 1 MHz. The largest rates to emerge from published R_1 dispersion curves across a range of material are to the best of our knowledge less than 1000 s^{-1}. These results confirm that FFC NMR may detect fluid in nanosized pores.

The shape and magnitude of $R_1(f)$ is shown to be sensitive to pore geometry at low frequency if relaxation is dominated by the motion of bulk fluid alone. The relaxation in most porous systems, however, is dominated by the surface fluid component. We complete calculations on realistic systems including the influence of pore-size variability. We find that, in principle, a FFC NMR measurement on a system containing a mixture of closed, channel, and planar pores would be characterized by three relaxation rate peaks at low frequency with closed pores yielding the highest rate and planar pores the lowest rate. However, due to the dominance of the surface fluid to the overall relaxation rate due to its proximity to relaxation centers and long diffusion time constant, the shapes of the dispersion curves are shown to be similar for each geometry. Therefore, if a system contained pores of a single geometry, it is concluded that it would not be possible to identify the pore geometry unless a reliable effective density of fixed relaxation centers was known *a priori*. Furthermore, it is shown that porous material containing a distribution of pore sizes leads to broad peaks in the $R_1(f)$ response.

The ratio T_1/T_2 is calculated for planar pores of thickness $h = 3$ nm, 30 nm, and 100 nm. T_1/T_2 exhibits a complex dependence on pore size h, surface mobility characterized by the surface diffusion time constant τ_ℓ, and NMR frequency f. T_1/T_2 tends to unity at low frequencies but is sensitive to f, h, and τ_ℓ at high frequency including the range 1–40 MHz normally employed in the conventional NMR experiments. It is shown that measurements of T_1/T_2 at 20 MHz in cement paste and hydrocarbon rock are consistent with a range of values of pore size h and τ_ℓ and therefore capture information on both characteristic pore size and surface mobility. Measurements of T_1/T_2 and distributions obtained from T_1-T_2 correlation measurements at different spot frequencies could potentially reveal both values and spread of characteristic pore size and surface diffusion time constant.

[1] D. N. Winslow and S. Diamond, J. Am. Ceram. Soc. **57**, 193 (1974).

[2] D. N. Winslow, J. M. Bukowski, and J. Francis Young, Cem. Concr. Res. **24**, 1025 (1994).

[3] S. Stock, N. Naik, A. Wilkinson, and K. Kurtis, Cem. Concr. Res. **32**, 1673 (2002).

[4] K. L. Scrivener, T. Füllmann, E. Gallucci, G. Walenta, and E. Bermejo, Cem. Concr. Res. **34**, 1541 (2004).

[5] J. J. Thomas, H. M. Jennings, and A. J. Allen, Cem. Concr. Res. **28**, 897 (1998).

[6] E. Fratini, S.-H. Chen, P. Baglioni, and M.-C. Bellissent-Funel, J. Phys. Chem. B **106**, 158 (2002).

[7] A. J. Allen, J. J. Thomas, and H. M. Jennings, Nat. Mater. **6**, 311 (2007).

[8] A. J. Allen and J. J. Thomas, Cem. Concr. Res. **37**, 319 (2007).

[9] H. N. Bordallo, L. P. Aldridge, and A. Desmedt, J. Phys. Chem. B **110**, 17966 (2006).

[10] J.-P. Korb, S. Xu, and J. Jonas, J. Chem. Phys. **98**, 2411 (1993).

[11] J.-P. Korb, M. Whaley-Hodges, and R. G. Bryant, Phys. Rev. E **56**, 1934 (1997).

[12] S. Godefroy, J.-P. Korb, M. Fleury, and R. G. Bryant, Phys. Rev. E **64**, 021605 (2001).

[13] F. Barberon, J.-P. Korb, D. Petit, V. Morin, and E. Bermejo, Phys. Rev. Lett. **90**, 116103 (2003).

[14] J.-P. Korb, M. Whaley Hodges, Th. Gobron, and R. G. Bryant, Phys. Rev. E **60**, 3097 (1999).

[15] R. Kimmich, Chem. Phys. **284**, 253 (2002).

[16] A. E. Sitnitsky, G. G. Pimenov, and A. V. Anisimov, J. Magn. Reson. **172**, 48 (2005).

[17] A. Plassais, M.-P. Pomiés, N. Lequeux, J.-P. Korb, D. Petit, F. Barberon, and B. Bresson, Phys. Rev. E **72**, 041401 (2005).

[18] L. Monteilhet, J.-P. Korb, J. Mitchell, and P. J. McDonald, Phys. Rev. E **74**, 061404 (2006).

[19] J.-P. Korb, P. J. McDonald, L. Monteilhet, A. G. Kalinichev, and R. J. Kirkpatrick, Cem. Concr. Res. **37**, 348 (2007).

[20] J.-P. Korb, New J. Phys. **13**, 035016 (2011).

[21] S. Stapf, R. Kimmich, and R.-O. Seitter, Phys. Rev. Lett. **75**, 2855 (1995).

[22] T. Zavada, R. Kimmich, J. Grandjean, and A. Kobelkov, J. Chem. Phys. **110**, 6977 (1999).

[23] P. J. McDonald, J.-P. Korb, J. Mitchell, and L. Monteilhet, Phys. Rev. E **72**, 011409 (2005).

[24] L. F. Gladden and J. Mitchell, New J. Phys. **13**, 035001 (2011).

[25] V.-V. Telkki, M. Yliniemi, and J. Jokisaari, Holzforschung **67**, 291 (2013).

[26] J.-P. Korb, B. Nicot, A. Louis-Joseph, S. Bubici, and G. Ferrante, J. Phys. Chem. C **118**, 23212 (2014).

[27] M. Fleury and M. Romero-Sarmiento, J. Pet. Sci. Technol. **137**, 55 (2016).

[28] J.-P. Korb, B. Nicot, and I. Jolivet, Microporous Mesoporous Mater. **269** 7 (2018).

[29] R. M. Steele, J.-P. Korb, G. Ferrante, and S. Bubici, Magn. Reson. Chem. **54**, 502 (2016).

[30] D. A. Faux, P. J. McDonald, and N. C. Howlett, Phys. Rev. E **95**, 033116 (2017).

[31] D. A. Faux and P. J. McDonald, Phys. Rev. E **95**, 033117 (2017).

[32] K. R. Brownstein and C. E. Tarr, Phys. Rev. A **19**, 2446 (1979).

[33] L. Ma, K. G. Taylor, P. D. Lee, K. J. Dobson, P. J. Dowey, and L. Courtois, Mar. Pet. Geol. **72**, 193 (2016).

[34] A. Abragam, *Principles of Nuclear Magnetism* (Clarendon Press, Oxford, 1961).

[35] J. Kowalewski and L. Maler, *Nuclear Spin Relaxation in Liquids: Theory, Experiments, and Applications* (CRC Press, Boca Raton, FL, 2017).

[36] D. Kruk, *Theory of Evolution and Relaxation of Multi-Spin Systems* (Arima, Bury St Edmunds, UK, 2007).

[37] D. A. Faux, D. K. Ross, and C. A. Sholl, J. Phys. C **19**, 4115 (1986).

[38] D. A. Faux, S.-H. P. Cachia, P. J. McDonald, J. S. Bhatt, N. C. Howlett, and S. V. Churakov, Phys. Rev. E **91**, 032311 (2015).

[39] D. A. Faux, P. J. McDonald, N. C. Howlett, J. S. Bhatt, and S. V. Churakov, Phys. Rev. E **87**, 062309 (2013).

[40] T. Bickel, Physica A **377**, 24 (2007).

[41] C. Sholl, J. Phys. C **14**, 447 (1981).

[42] A. Avogadro and M. Villa, J. Chem. Phys. **66**, 2359 (1977).